Mesoscopic model to simulate the mechanical behavior of reinforced concrete members affected by corrosion

P.J. Sánchez[1−3], A.E. Huespe[1], J. Oliver[2] and S. Toro[3]

[1] International Center for Computational Methods in Engineering (CIMEC)
Güemes 3450, 3000
Santa Fe, Argenina
psanchez@intec.unl.edu.ar
ahuespe@intec.unl.edu.ar

[2] Technical University of Catalonia (UPC)
Campus Nord, modul C-I
Gran Capitán s\n, 08034
Barcelona, España
xavier.oliver@upc.es

[3] GIMNI - Universidad Tecnológica Nacional
Facultad Regional Santa Fe
Lavaise 610, 3000
Santa Fe, Argentina
storo@frst.utn.edu.ar

Key Words: *reinforced concrete structures, corrosion, finite elements with embedded strong discontinuities, bond stress degradation, contact elements.*

ABSTRACT

In this contribution, a finite element methodology devised to simulate the structural deterioration of corroded reinforced concrete members is presented. The proposed numerical strategy has the ability to reproduce many of the well-known (undesirable) mechanical effects induced by corrosion processes in the embedded steel bars, as for example: expansion of the reinforcements due to the corrosion product accumulation, damage and cracking patterns distribution in the surrounding concrete, degradation of steel-concrete bond stress transfer, net area reduction in the reinforcement fibers and, mainly, the influence of all these mentioned mechanisms on the structural load carrying capacity predictions.

At numerical level, each component of the RC structure is represented by means of a suitable FE formulation. For the concrete, a cohesive model based on the *Continuum Strong Discontinuity Approach* (*CSDA*) is used. Steel bars are considered by means of an elasto-plastic model. The interface is simulated using contact-friction elements, with the friction degradation as a function of the degree of corrosion attack. Two different (and coupled) mesoscopic analyzes are considered in order to describe the main physical phenomena that govern the problem: *(i)* analysis at cross section level and *(ii)* analysis at structural member level.

The resultant mechanical model can be used either to simulate generalized or localized reinforcement corrosion. Experimental and previous numerical results, obtained from the available literature, are used to validate the proposed strategy.

1 Introduction

Reinforced Concrete structures (RC structures) are widely used across the world. Many reasons justify the broad acceptation of such constructive technology, as it is discussed in standard textbooks and several concrete building codes. Nevertheless, they have a *Limited Service Life* due to serious age-related degradation mechanisms that affect its durability and the long-term structural reliability. This fact forces the engineers to study, and to understand, the most important sources of damage. In this context, the corrosion of the embedded reinforcement steel bars is identified as one of the most critical aspects influencing the RC service life. The problem must be carefully analyzed because it could cause premature deterioration and, sometimes, the necessity of expensive repairs, strengthening, or even the demolition and replacement of existing RC structures [1].

The corrosion phenomenon observed in RC elements is formally described as an electro-chemical process. In general, the use of high quality materials jointly with appropriate control/constructive techniques, guarantee the formation of a highly alkaline layer at the steel-concrete interface [2]. These two conditions can efficiently prevent, or minimize, the corrosion effects in the reinforcement bar because they keep a chemically stable environment. However, they cannot be always preserved during the complete service life, specially when RC structures are exposed to an aggressive medium or when external solicitations degrade the cover concrete of the reinforcements. Typically, two chemical (undesirable) scenarios can be expected in an RC structure: the carbonation process what induces a mechanism of *Generalized Corrosion*, and the penetration of chloride ions causing, primarily, *Localized Corrosion*.

The economic importance and the technological consequences of this problem have motivated, in the last years, numerous research programs. Thus, they can be mentioned many experimental works reporting the unfavorable corrosion effects on RC elements, see for example [3, 4, 5, 6, 7, 8, 9, 10, 11, 12], and also analytical studies and numerical models ([13, 14, 15, 16, 17, 18, 19, 20]) addressed to understand this complex degradation mechanism.

From the wide spectrum of phenomena involved in the reinforcement fiber corrosion process, in the present work we are only interested in those aspects related with the mechanical problem. In this context, we present a numerical model suitable to simulate the evolution of the mechanical degradation mechanisms of RC structural members caused by the reinforcement fiber corrosion. Phenomena such as: *(i)* expansion of the corroded bars, *(ii)* distribution of crack patterns, *(iii)* loss of steel-concrete bond adherence, *(iv)* net area reduction of the steel fiber cross section and *(v)* the effects of the above mentioned mechanisms on the structural load carrying capacity, can be analyzed as a function of the reinforcement corrosion degree. Therefore, the model makes possible to determine the influence and sensitivity of this key variable, the reinforcement corrosion level, in the structural deterioration problem.

The proposed numerical strategy can be applied to beams, columns, slabs, etc., through two succesive and coupled mesoscopic mechanical analyzes, as follows:

(i) At the structural member cross section level, we simulate the reinforced fiber expansion due to the volume increase of the steel bars as a consequence of corrosion product accumulation (see Section 2). Damage distribution and cracking patterns in the concrete bulk and cover is evaluated, which (indirectly) defines the concrete net section loss in the structural member.

(ii) A second mesoscopic model at the structural level, considering the results of the previous analysis, evaluates the mechanical response of the structural member subjected to an external loading system (see Section 3). This evaluation determines the global response and the macroscopic mechanisms of failure.

Section 4 presents a consistent coupling between the two analyzes in points *(i)* and *(ii)*. Finally, applications of such strategy to determine limit loads in RC beams, as a function of corrosion attack depth, are shown. The obtained quantitative structural limit load predictions are compared with available experimental results, standard code procedures (based on simpler models) and numerical estimation previously proposed.

2 Cross section analysis of the structural member (expansion mode)

Let us consider the cross section of an arbitrary RC structural member, as displayed in Figure 1-(b), whose reinforcement fibers are experiencing a corrosion process. The products derived from the steel bar corrosion, such as ferric oxide rust, reduce the net steel area and accumulate causing volumetric expansion of the bars (see Figure 1-(a)), what induces a high hoop tensile stress state in the surrounding concrete. As a consequence the cover concrete undergoes a damage and a degradation process displaying two typical fracture patterns: *(i)* inclined cracks and *(ii)* delamination cracks, as observed in Figure 1-(c) (see also [21]). Obviously, these induced cracks can increase the rate of corrosion process in the structural member.

In this Section, we present a numerical model based on a finite element technique that is specially addressed to study this phenomenon. The two-dimensional plane strain mesoscopic model, as idealized in Figure 1-(b), considers three different domains of analysis: *(i)* the concrete matrix, *(ii)* the steel reinforcement bars and *(iii)* the steel-concrete interface. Each of them are characterized by a different constitutive response and FE technology that take into account the main mechanisms involved in the corrosion process.

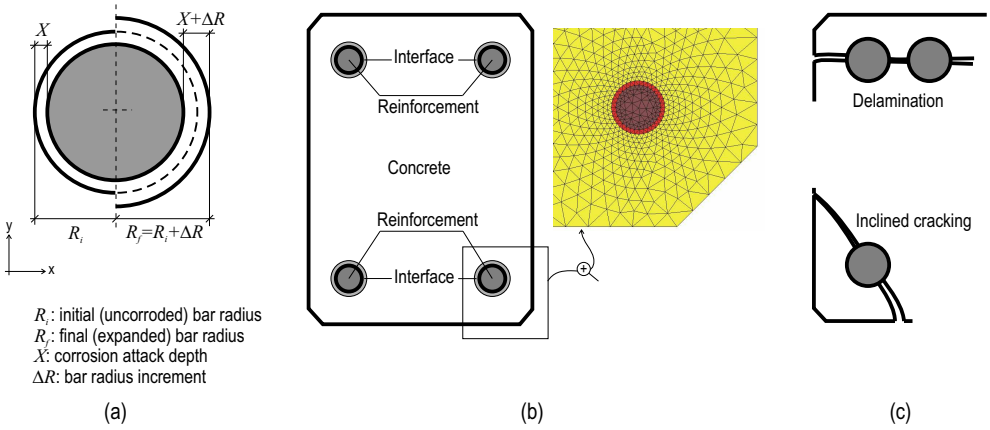

Figure 1: RC structural member cross section. Plane strain mesoscopic 2D model: (a) Corrosion-expansion mechanism. (b) Numerical model idealization. (b) Typical pattern of cracks.

2.1 The concrete model

The model adopted for analyzing the concrete matrix constitutive response is an isotropic continuum damage model regularized by means of the *Continuum Strong Discontinuity Approach* (*CSDA*), as described in [22]. It has been shown that this technique is robust enough and flexible to simulate different patterns of distributed cracks in solids, similar to that observed in RC structures undergoing advanced deterioration stages. Here we only summarize the main features of this model. Additional theoretical details can be obtained elsewhere [23, 24].

- *(i)* The macroscopic discontinuities arising in a solid, such as cracks or fractures, are mathematically described by a strong discontinuity kinematics.

  Let be given a body Ω experiencing a strong discontinuity (displacement jumps) across the surface S (see Figure 2). The surface S divides the body in two disjunct domains Ω^+ and Ω^-. The displacement $\boldsymbol{u}(\boldsymbol{x})$ and the compatible strain field $\boldsymbol{\varepsilon}(\boldsymbol{x})$, in Ω, can be written as:

$$\boldsymbol{u}(\boldsymbol{x}) = \overbrace{\overline{\boldsymbol{u}}(\boldsymbol{x})}^{continuous} + \overbrace{H_S(\boldsymbol{x})\,[\![\boldsymbol{u}]\!](\boldsymbol{x})}^{discontinuous} \quad ; \quad H_S(\boldsymbol{x}) = \begin{cases} 1 & \forall \boldsymbol{x} \in \Omega^+ \\ 0 & \forall \boldsymbol{x} \in \Omega^- \end{cases} \tag{1}$$

$$\boldsymbol{\varepsilon}(\boldsymbol{x}) = \nabla^{sym}\boldsymbol{u}(\boldsymbol{x}) = \underbrace{\overline{\boldsymbol{\varepsilon}}(\boldsymbol{x})}_{regular} + \underbrace{\delta_S(\boldsymbol{x})\,\big([\![\boldsymbol{u}]\!] \otimes \boldsymbol{n}\big)^{sym}}_{singular} \tag{2}$$

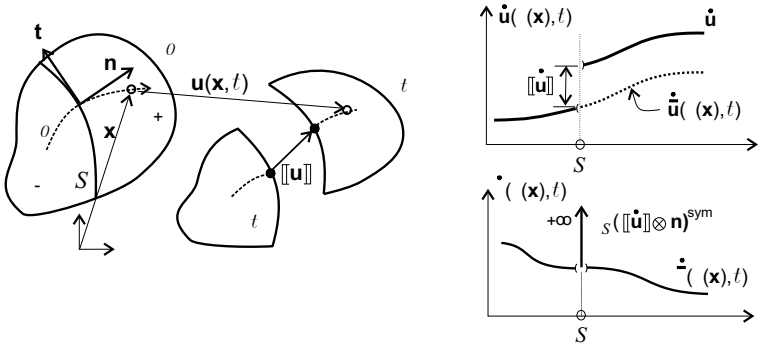

Figure 2: Strong discontinuity kinematics.

where $\overline{\boldsymbol{u}}(\boldsymbol{x})$ is a continuous function in Ω, $[\![\boldsymbol{u}]\!](\boldsymbol{x})$ represents the displacement jump across the discontinuity S and $H_S(\boldsymbol{x})$ is the Heaviside's step function. The strain field shows a singular term, the second one in equation (2), given by the Dirac's delta distribution $\delta_S(\boldsymbol{x})$.

- *(ii)* Concrete can be quite appropriately modeled by means of an isotropic continuum damage model equipped with a regularized strain softening in order to make possible the onset of material instabilities, strain localization and crack propagation. Table 1 defines this material model, where damage in tension and compression is possible, but different ultimate limit stresses are used [25]. There, $\boldsymbol{\sigma}$ and $\boldsymbol{\varepsilon}$ represent the stress and strain tensors, q and r are internal variables defining the standard damage variable $d = 1 - \frac{q}{r}$, the elastic material parameters E, λ and μ are the Young's modulus and the Lamé's coefficients. Also we define σ_u^C and σ_u as the compressive and tensile limit strength, respectively.

  The compatibility between the strong discontinuity kinematics, eqs. (1)-(2), and the continuum damage material model is performed by introducing an intrinsic softening modulus $\bar{H} = \delta_S\, H$, whose value is computed from the classical parameters used in the Fracture Mechanics context: $\bar{H} = f(\sigma_u, G_f, E)$, where G_f is the concrete fracture energy. This intrinsic modulus allows defining a bounded stress state in S through the standard continuum damage model of Table 1, even when the strains $\boldsymbol{\varepsilon}$ are defined by a singular term, see equation (2).

- *(iii)* The vector traction continuity across the discontinuity interface S, equilibrium condition, requires that:

$$\boldsymbol{t}_S = \boldsymbol{\sigma}_S \cdot \boldsymbol{n} = \boldsymbol{\sigma}_{\Omega^+} \cdot \boldsymbol{n} \tag{17}$$

  When the strong discontinuity kinematics (1)-(2) is consistently introduced in this continuum setting, a cohesive model $\boldsymbol{t}_S = f([\![\boldsymbol{u}]\!])$ is automatically projected onto the interface S [26]. This traction-separation cohesive law governs the crack opening evolution in the strong discontinuity regime.

- *(iv)* The previously discussed model is numerically implemented by using a finite element technique based on embedded strong discontinuities. Basically, this methodology consists of enriching the standard continuous displacement modes adding enhanced discontinuous ones and, consequently, additional degrees of freedom. It makes possible to capture the crack trajectory inside the finite elements irrespective of the size and orientation of them. In particular, the E-FEM technology [27] has been adopted in the present work, see Figure 3. This strategy permits the condensation of the extra discontinuous modes at elemental level and, therefore, the additional d.o.f. does not enlarge the size of the final equation system.

Summarizing, the non-linear analysis of the concrete response is performed with a continuum format by using standard stress-strain constitutive descriptions such as the presented in Table 1.

Elastic stress-strain relationship

$$\boldsymbol{\sigma} = \frac{q(r)}{r}\,\boldsymbol{C}^e : \boldsymbol{\varepsilon} = [1 - d(r)]\,\overbrace{\boldsymbol{C}^e : \boldsymbol{\varepsilon}}^{\overline{\boldsymbol{\sigma}}} \tag{3}$$

$$\boldsymbol{C}^e = \lambda\,(\mathbb{1}\otimes\mathbb{1}) + 2\mu\,\mathbb{I} \quad \text{(Isotropic elastic tensor)} \tag{4}$$

$$\mathbb{1} = \delta_{ij}\,(\boldsymbol{e}_i \otimes \boldsymbol{e}_j) \tag{5}$$

$$\mathbb{I} = \frac{1}{2}\,(\delta_{ik}\delta_{jl} + \delta_{il}\delta_{jk})\,(\boldsymbol{e}_i \otimes \boldsymbol{e}_j \otimes \boldsymbol{e}_k \otimes \boldsymbol{e}_l) \tag{6}$$

Damage criterion

$$\phi(\boldsymbol{\sigma}, q) = \tau_{\boldsymbol{\sigma}} - q \leq 0 \tag{7}$$

$$\tau_{\boldsymbol{\sigma}} = \chi\sqrt{\boldsymbol{\sigma} : (\boldsymbol{C}^e)^{-1} : \boldsymbol{\sigma}} = \chi\,[1 - d(r)]\,\sqrt{\overline{\boldsymbol{\sigma}} : (\boldsymbol{C}^e)^{-1} : \overline{\boldsymbol{\sigma}}} \tag{8}$$

$$\chi = \frac{\sum_{i=1}^{i=3}\langle\overline{\sigma}_i\rangle}{\sum_{i=1}^{i=3}|\overline{\sigma}_i|}\left[1 - \frac{1}{n_\sigma}\right] + \frac{1}{n_\sigma} \tag{9}$$

$$n_\sigma = \frac{\sigma_u^C}{\sigma_u} \tag{10}$$

$$\langle\bullet\rangle = \frac{1}{2}\{\bullet + \|\bullet\|\} \tag{11}$$

$$\overline{\sigma}_i \equiv \text{principal values of } \overline{\boldsymbol{\sigma}} \tag{12}$$

Softening evolution law

$$\dot{r} = \gamma \quad ; \quad r_0 = r|_{t=0} = \frac{\sigma_{\boldsymbol{u}}}{\sqrt{E}} \tag{13}$$

$$\dot{q} = H(r)\,\dot{r} \quad ; \quad q_0 = q|_{t=0} = r_0 \tag{14}$$

$$(\gamma \equiv \text{consistency parameter}) \tag{15}$$

Loading-unloading complementarity conditions

$$\phi(\boldsymbol{\sigma}, q) \leq 0 \quad ; \quad \gamma \geq 0 \quad ; \quad \gamma\,\phi(\boldsymbol{\sigma}, q) = 0 \tag{16}$$

Table 1: Continuum damage model for the concrete response simulation.

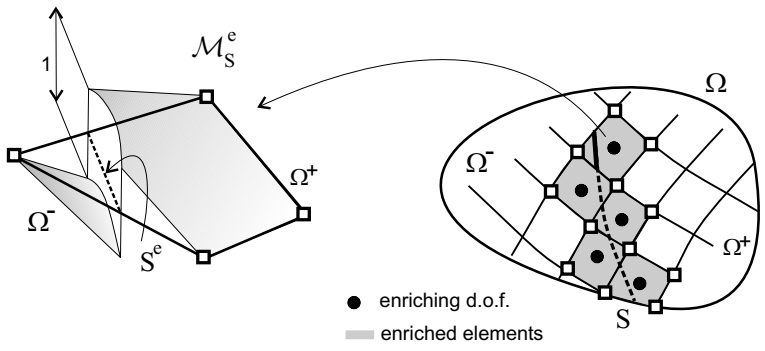

Figure 3: Embedded finite elements whit internal enhanced d.o.f. (E-FEM technology).

2.2 The steel bar model

A standard linear elastic (isotropic) constitutive behavior is assumed for the steel bars. The expansion effect, due to the corrosion phenomenon, is considered through a (pseudo) volumetric initial deformation mode $\boldsymbol{\varepsilon}^0$.

Let us assume that the cross section of a typical RC member is contained in the the x-y plane, see Figure 1. Making use of the standard Voigt's notation for tensors and assuming a plane strain state, the total strains can be expressed as the superposition of two terms:

$$\boldsymbol{\varepsilon} = \nabla^{sym}\boldsymbol{u}(\boldsymbol{x}) = \begin{bmatrix} \varepsilon_{xx} \\ \varepsilon_{yy} \\ \gamma_{xy} \\ \varepsilon_{zz} \end{bmatrix} = \begin{bmatrix} \varepsilon_{xx} \\ \varepsilon_{yy} \\ \gamma_{xy} \\ 0 \end{bmatrix} = \overbrace{\begin{bmatrix} \frac{1}{E}(\sigma_{xx} - \nu\sigma_{yy} - \nu\sigma_{zz}) \\ \frac{1}{E}(\sigma_{yy} - \nu\sigma_{zz} - \nu\sigma_{xx}) \\ 2(\frac{1+\nu}{E})\,\sigma_{xy} \\ \frac{1}{E}(\sigma_{zz} - \nu\sigma_{xx} - \nu\sigma_{yy}) \end{bmatrix}}^{\boldsymbol{\varepsilon}^e} + \overbrace{\begin{bmatrix} \mathcal{D} \\ \mathcal{D} \\ 0 \\ 0 \end{bmatrix}}^{\boldsymbol{\varepsilon}^0} \tag{18}$$

where $\mathcal{D}$ is the value of the dilatational component due to the corrosion products and $\boldsymbol{\varepsilon}^e$ the elastic part. Note that the dilatational coefficient is not included in the zz component of $\boldsymbol{\varepsilon}^0$ because does not exist any expansion effect in the axial direction of the bars.

Taking into account the classical elastic relation $\boldsymbol{\sigma} = \boldsymbol{C}^e : \boldsymbol{\varepsilon}^e$, the stress response can be computed as follows:

$$\boldsymbol{\sigma} = \begin{bmatrix} \sigma_{xx} \\ \sigma_{yy} \\ \tau_{xy} \\ \sigma_{zz} \end{bmatrix} = \begin{bmatrix} \alpha & \beta & 0 & \beta \\ \beta & \alpha & 0 & \beta \\ 0 & 0 & \gamma & 0 \\ \beta & \beta & 0 & \alpha \end{bmatrix} \begin{bmatrix} \varepsilon_{xx} - \mathcal{D} \\ \varepsilon_{yy} - \mathcal{D} \\ \gamma_{xy} \\ 0 \end{bmatrix} \tag{19}$$

where we have defined the elastic parameters: $\alpha = \frac{E(1-\nu)}{(1+\nu)(1-2\nu)}$, $\beta = \frac{E\nu}{(1+\nu)(1-2\nu)}$ and $\gamma = \frac{E}{2(1+\nu)}$.

The increment of the bar radius, from the initial value R_i to the (corroded) final one R_f ($\Delta R = (R_f - R_i)$), see Figure 1-(a), depends on the corrosion attack depth X, which is an experimentally determined value. Therefore, $R_f = \hat{R}_f(X)$ and the dilatation parameter $\mathcal{D}$ can be estimated as a function of X:

$$\mathcal{D} \approx \frac{\hat{R}_f^2(X) - R_i^2}{2R_i^2} \tag{20}$$

Note that, in view of equation (20), the depth of corrosion attack (X) is a fundamental input data of the present model.

During the numerical simulation process, the total magnitude of dilatation $\mathcal{D}$ is applied incrementally, i.e. if nt times steps are required to perform the complete non-linear analysis, a (pseudo) volumetric expansion state $\Delta\boldsymbol{\varepsilon}^0 = \frac{\mathcal{D}}{nt}\,[1\,1\,0\,0]^T$ is applied per time step, on each steel element.

2.3 The steel-concrete interface model (contact element)

A phenomenological observation of the mechanisms taking place in the steel-concrete interface, suggests that there exists a limit value for the shear stress transference (maximum adherence stress τ_{max}) that depends on several factors: bar diameter, bar surface texture, confining effects, corrosion level, etc. Eventually, when high expansion values in the steel are reached, the separation between both materials (steel and concrete) must be expected.

These effects have important consequences in the concrete fracture pattern prediction, what motivates the introduction of contact finite elements in order to simulate appropriately the steel-concrete interface,

as shown in Figure 4-(a). The contact linear triangular element adopted in the present model, to simulate the interface steel-concrete interaction, has been taken from [28], where additional details about its formulation can be obtained.

In every contact finite element, it is defined a local cartesian system $\{\boldsymbol{\eta}, \boldsymbol{t}\}$, where $\boldsymbol{\eta}$ is the unit vector normal to the contact surface. The strains are evaluated from the nodal displacement, as it is done in standard finite elements. The mechanical response of the contact-friction model is expressed by means of the following constitutive law:

$$\boldsymbol{\sigma} = \Psi(g)\left[\overbrace{\sigma_{\eta\eta}(\varepsilon_{\eta\eta})\,(\boldsymbol{\eta}\otimes\boldsymbol{\eta})}^{\text{linear-elastic}} + \overbrace{\tau_{\eta t}(\varepsilon_{\eta t})\,[(\boldsymbol{\eta}\otimes\boldsymbol{t}) + (\boldsymbol{t}\otimes\boldsymbol{\eta})]}^{\text{elasto-plastic}}\right] \tag{21}$$

where the scalar step function $\Psi(g)$ is:

$$\Psi(g) = \begin{cases} 1 & ; \quad \text{if} \quad g < 0 \\ 0 & ; \quad \text{if} \quad g \geq 0 \end{cases} \tag{22}$$

and the gap function, $g(\varepsilon_{\eta\eta})$, is computed as:

$$g(\varepsilon_{\eta\eta}) = h^e\,\varepsilon_{\eta\eta} \tag{23}$$

h^e being the length of the finite element in the $\boldsymbol{\eta}$ direction.

The normal contact stress, $\sigma_{\eta\eta}$, is obtained as a function of the constant strain component $\varepsilon_{\eta\eta}$ ($\varepsilon_{\eta\eta} = \boldsymbol{\eta}\cdot\boldsymbol{\varepsilon}\cdot\boldsymbol{\eta}$), following a 1D linear elastic law (see Figure 4-(c)). The friction stress component, $\tau_{\eta t}$, is determined as a function of the constant shear strain component $\varepsilon_{\eta t}$ ($\varepsilon_{\eta t} = \boldsymbol{\eta}\cdot\boldsymbol{\varepsilon}\cdot\boldsymbol{t}$) by means of a classical 1D elasto-plastic constitutive model, as detailed in Table 2 (see also Figure 4-(d)). The elasto-plastic model of Table 2 only applies when $\Psi(g) = 1$, otherwise no evolution of plastic flow is considered.

Summarizing, the proposed contact-friction model is characterized by four parameters: the normal stiffness ($K_{\eta\eta}$) working as a penalty parameter, the shear stiffness ($K_{\eta t}$), the maximum adherence stress (τ_{max}) and the hardening/softening shear modulus ($\overline{K}$).

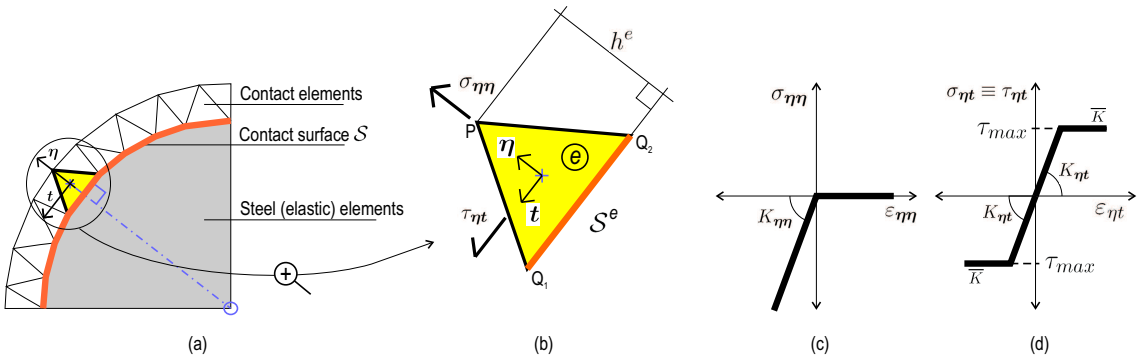

Figure 4: Contact finite element at the interface: (a) Representative scheme. (b) Typical contact element. (c) Scheme of the constitutive law for the contact normal stress $\sigma_{\eta\eta}$. (d) Scheme of the constitutive law for the friction shear stress $\tau_{\eta t}$.

Incremental elastic stress-strain relationship

$$\dot{\tau}_{\eta t} = K_{\eta t}\left(\dot{\varepsilon}_{\eta t} - \dot{\varepsilon}^{p}_{\eta t}\right) \tag{24}$$

Yield condition

$$\phi(\tau_{\eta t}, \alpha) = |\tau_{\eta t}| - (\tau_{max} + \overline{K}\alpha) \leq 0 \tag{25}$$

Flow rule and hardening/softening evolution law

$$\dot{\varepsilon}^{p}_{\eta t} = \gamma \, sign(\tau_{\eta t}) \tag{26}$$

$$\dot{\alpha} = \gamma \tag{27}$$

($\gamma \equiv$ plastic multiplier)

($\alpha \equiv$ accumulated equivalent plastic strain)

Loading-unloading complementarity conditions

$$\phi(\tau_{\eta t}, \alpha) \leq 0 \quad ; \quad \gamma \geq 0 \quad ; \quad \gamma\,\phi(\tau_{\eta t}, \alpha) = 0 \tag{28}$$

Table 2: Basic equations for 1D elasto-plastic friction model ($\tau_{\eta t}$ shear stress).

3 Mesoscopic model to simulate the structural load carrying capacity (flexure mode)

The model of Section 2 provides qualitative information related to the concrete degradation mechanisms due to the steel expansion. Nevertheless, it does not give additional information about the mechanical behavior of a deteriorated RC structure subjected to external loads.

In this Section we introduce a 2D mesoscopic model for the quantitative prediction of residual load carrying capacity of corroded RC members, where each component of the structure (concrete, steel and steel-concrete interface) is independently represented. An idealized scheme of the adopted discrete model, applied to an RC beam, can be observed in Figure 5.

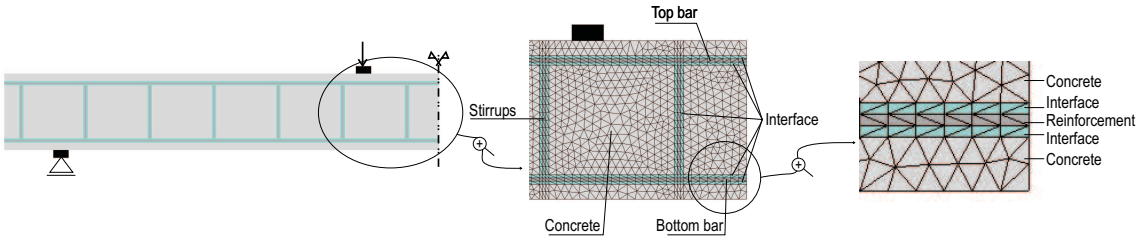

Figure 5: Plane stress beam mesoscopic 2D model.

The present (plane stress) mesoscopic strategy has many similar features with the (plane strain) mesoscopic model of the previous Section (2). In fact, the concrete model we adopt here is the *CSDA*, that discussed in sub-Section 2.1, with identical enhanced finite elements technology, isotropic (tension-compression) continuum constitutive damage model and crack propagation scheme. Furthermore, a similar procedure to that described in sub-Section 2.3 is here adopted for the steel-concrete interface model. Note that, in the present case, the contact elements provide the necessary coupling between the concrete matrix and the reinforcements acting as top/bottom longitudinal bars and stirrups. Consequently, a consistent definition of the unit normal vector, $\boldsymbol{\eta}$, is required in each contact finite element.

The mechanical behavior of the steel bars is simulated with an elasto-plastic model, which is briefly discussed in the following sub-Section.

3.1 Elasto-plastic model for the longitudinal steel reinforcement bars

The steel bar response is characterized by a 2D finite element model. Each finite element has associated a local normalized cartesian basis $\{\boldsymbol{\eta}, \boldsymbol{t}\}$. The vector $\boldsymbol{\eta}$ is computed such that it is orthogonal to the longitudinal bar axis, see Figure 6-(a). The reinforcement mechanical behavior reproduces a 1D standard elasto-plastic model in the σ_{tt} normal stress component, while the remaining stress tensor components behave elastically, assuming a Poisson relation $\nu = 0$.

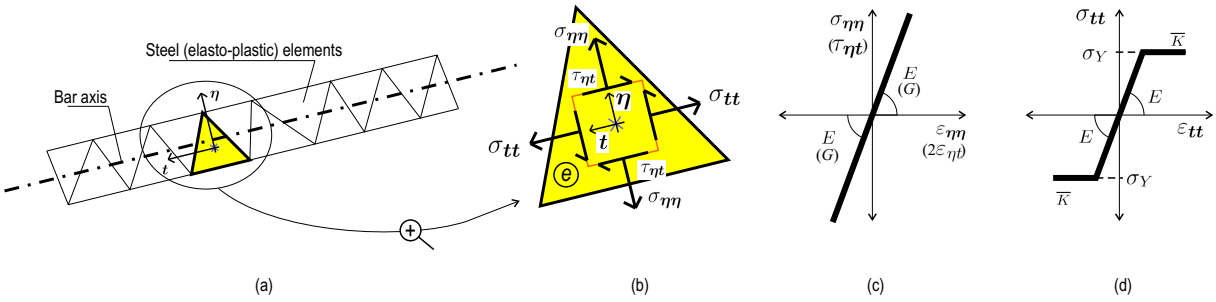

Figure 6: Elasto-plastic reinforcement element: (a) Representative scheme. (b) Typical steel element. (c) Scheme of the constitutive law for $\sigma_{\eta\eta}$ and $\tau_{\eta t}$ stresses. (d) Scheme of the constitutive law for σ_{tt} stress.

Thus, the stress tensor is given by:

$$\boldsymbol{\sigma} = \underbrace{\sigma_{\eta\eta}\,(\boldsymbol{\eta}\otimes\boldsymbol{\eta}) + \tau_{\eta t}\left[(\boldsymbol{\eta}\otimes\boldsymbol{t}) + (\boldsymbol{t}\otimes\boldsymbol{\eta})\right]}_{\text{linear-elastic}} + \underbrace{\sigma_{tt}\,(\boldsymbol{t}\otimes\boldsymbol{t})}_{\text{elasto-plastic}} \tag{29}$$

where $\sigma_{\eta\eta} = E\,\varepsilon_{\eta\eta}$, $\tau_{\eta t} = \tau_{t\eta} = G\,2\,\varepsilon_{\eta t}$ ($G = \frac{E}{2}$ being the shear modulus), see Figure 6-(c), and σ_{tt} is given by the standard 1D plasticity model shown in Table 3, see also Figure 6-(d).

Incremental elastic stress-strain relationship

$$\dot{\sigma}_{\boldsymbol{tt}} = E\,(\dot{\varepsilon}_{\boldsymbol{tt}} - \dot{\varepsilon}^{p}_{\boldsymbol{tt}}) \tag{30}$$

Yield condition

$$\phi(\sigma_{\boldsymbol{tt}}, \alpha) = |\sigma_{\boldsymbol{tt}}| - (\sigma_Y + \overline{K}\alpha) \leq 0 \tag{31}$$

Flow rule and hardening/softening evolution law

$$\dot{\varepsilon}^{p}_{\boldsymbol{tt}} = \gamma\, sign(\sigma_{\boldsymbol{tt}}) \tag{32}$$

$$\dot{\alpha} = \gamma \tag{33}$$

($\gamma \equiv$ plastic multiplier)

($\alpha \equiv$ accumulated equivalent plastic strain)

Loading-unloading complementarity conditions

$$\phi(\sigma_{\boldsymbol{tt}}, \alpha) \leq 0 \quad ; \quad \gamma \geq 0 \quad ; \quad \gamma\,\phi(\sigma_{\boldsymbol{tt}}, \alpha) = 0 \tag{34}$$

Table 3: Basic equations for 1D elasto-plastic steel model ($\sigma_{\boldsymbol{tt}}$ normal stress).

Summarizing, the proposed elasto-plastic model is characterized by three parameters: the Young's modulus (E), the uniaxial yield stress (σ_Y) and the hardening/softening modulus ($\overline{K}$).

4 Coupling strategy between the cross section and the structural member model

Figure 7 shows an idealized scheme of the strategy adopted in this work to couple the two models presented in the previous Sections, i.e. the cross section analysis and the structural member analysis.

As it can be observed in the figure we transfer, from one domain of analysis to the other, the average value of the damage variable "d" across horizontal slices of the cross section model. This projection is consistent because both analysis use the same continuum isotropic damage model for simulating the concrete domain. Thus, the final degradation state of concrete induced by the steel bar volumetric deformation process, is considered to be the initial damage condition for the subsequent structural analysis. This means that we are assuming that the two mesoscopic models are coupled in only one direction, neglecting the structural load effects on the concrete damage evaluation determined in the cross section analysis. A complete coupling between these mechanisms could be obtained by using a 3D model with identical ingredients to that presented in the preceding Section.

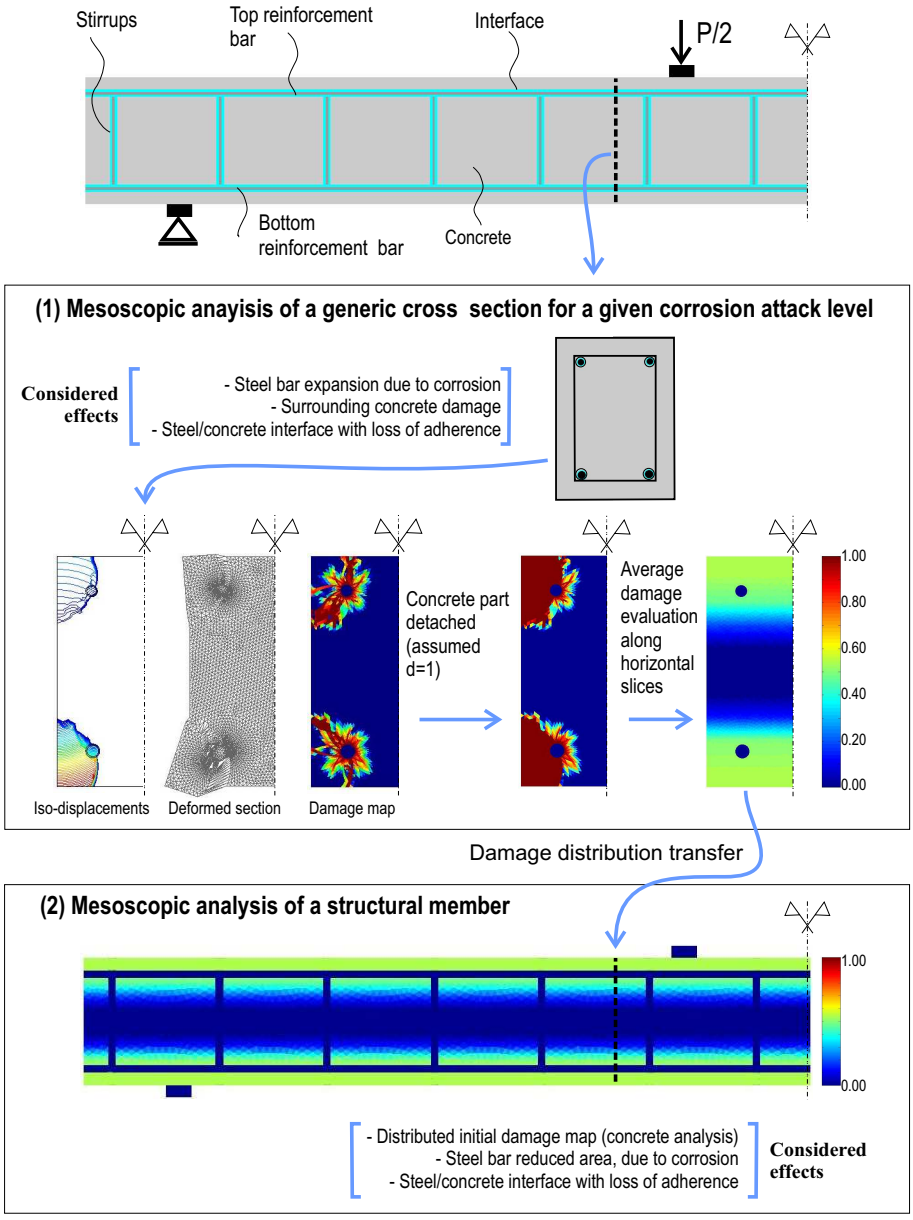

Figure 7: Coupling strategy between the cross section analysis and the structural member analysis.

Note that in the present strategy, and in contrast to other simpler models previously proposed for corroded RC members, neither ad-hoc assumptions about reductions in the net cross section area of the

concrete nor empirical modifications in the definition of its constitutive behavior are introduced in order to simulate the degradation by corrosion in the concrete matrix. This complex phenomenon is taken into account in a unique constitutive scenario (continuum damage model) performing a consistent mapping of the damage variable between the two level of analysis.

5 Numerical results

In this Section, a set of numerical simulations is addressed in order to test the performance of the described finite element formulations. Two types of RC beams have been analyzed, we call them: Beam type 11 and 31 (additional indices will be added to indicate different corrosion levels). The geometry and boundary conditions of the examples are shown in Figure 8. Table 4 presents additional information on the geometry and material data. The differences between both beam types are the reinforcement arrangements (steel ratios of top/bottom bars and stirrups separations).

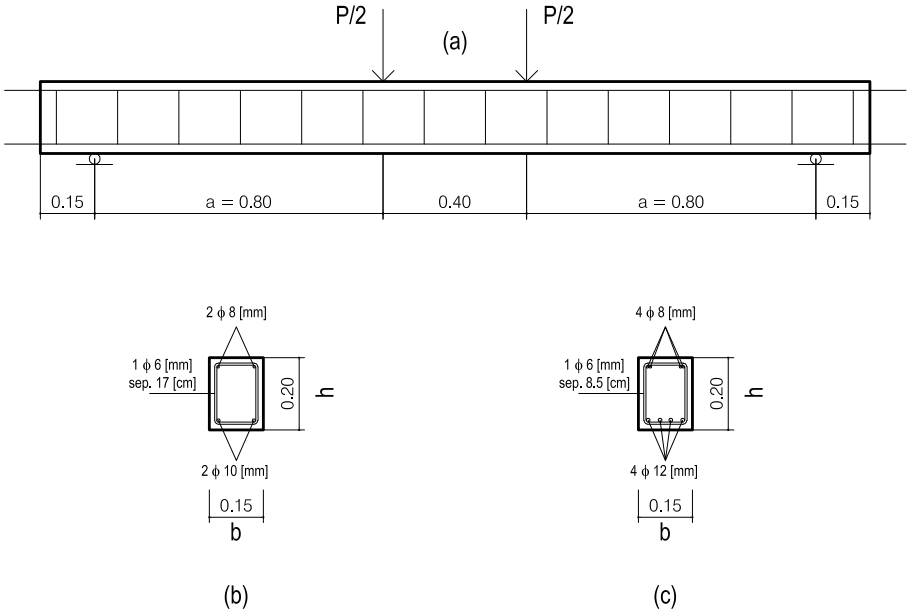

Figure 8: RC beams: (a) Dimensions and boundary conditions (length in [m], except the specified ones). (b) Cross section scheme for beam type 11 ($\approx 0.5\%$ steel-concrete ratio). (c) Cross section scheme for beam type 31 ($\approx 1.5\%$ steel-concrete ratio).

(1) Beam type	(2) Dimensions l × b ×h [m]	(3) Top bars number/diameter [mm]	(4) Bottom bars number/diameter [mm]	(5) Stirrups diameter/spacing [mm]	(6) Concrete strength: σ_u^C [MPa]	(7) Steel yield stress: σ_Y [MPa]
11	$2.00 \times 0.15 \times 0.20$	$2\,\phi 8$	$2\,\phi 10$	$\phi 6/170$	$50 - 34$	575
31	$2.00 \times 0.15 \times 0.20$	$4\,\phi 8$	$4\,\phi 12$	$\phi 6/85$	$49 - 37$	575

Table 4: RC beams. Material description (taken from [19]).

For these specimens, experimental results are available, see Rodriguez et al. [4, 5]. In these works a process of accelerated corrosion was induced by applying a constant anodic current density of $100\,[\mu A/cm^2]$ in the embedded steel bars and also by using a contaminated concrete mixture with calcium chloride, which produces a generalized corrosion phenomenon. Table 5 shows some experimental measurements of the attack depth X, for different levels of corrosion and types of reinforcement.

Coronelli et al. [19] have presented a numerical mesoscopic 2D model for corroded RC elements, which has been validated with the above mentioned experimental results of Rodriguez et al. [4]. In the present work, we follow very close the guidelines and material characterization reported in [19].

(1) Beam denomination	(2) Bottom bars attack: X_B [mm]	(3) Top bars attack: X_T [mm]	(4) Stirrup attack: X_S [mm]	(5) τ_{max} [MPa]
$11-1$	—	—	—	6.86
$11-4$	0.45	0.52	0.39	4.10
$11-5$	0.36	0.26	0.37	4.13
$11-6$	0.70	0.48	0.66	4.04
$31-1$	—	—	—	7.82
$31-3$	0.30	0.20	0.35	5.12
$31-4$	0.48	0.26	0.50	5.06

Table 5: Experimental corrosion attack measures [4, 5] and residual adherence stress τ_{max}[3]. Beam type 11 and 31 (taken from [19]).

5.1 General aspects of the numerical simulations

Triangular finite elements with linear interpolation have been adopted for all the tests. In particular, enhanced strong discontinuity triangular elements are used for the concrete material.

Each numerical problem is solved by imposing an arc-length displacement-based control strategy. In the plane strain expansion tests, the control is applied over the dilatation variable $\mathcal{D}$. For the bending examples, we control the vertical displacement of the beam central point.

A special mention deserves the numerical algorithm used to integrate the non-linear constitutive models. In this context, a very robust scheme is adopted, namely the *Impl-Ex* method [28]. It allows to obtain efficient solutions, even in really complex situations.

In order to optimize the computational resources and computing effort, we have taken advantage of as many symmetry conditions as possible.

The material parameter characterization considers the following aspects:

- The concrete compressive limit strength, σ_u^C, is given in Table 4, column 6 (the first figure corresponds to the concrete used in the not corroded beams and the second one to the contaminated concrete mixture). The ultimate concrete tensile stress, σ_u, is assumed as: $\sigma_u = 0.10\,\sigma_u^C$. Other material properties for the concrete, as for example Young's modulus, Poisson's ratio, fracture energy and softening modulus, are adopted by setting standard values (and previously used by the authors in the solution of similar fracture mechanics problems, see for example [27]).

- The contact model depends on the ultimate adherence stress $\tau_{max}(X)$. Column 5 of Table 5 (see also Rodriguez et al. 1994 [3]) provides a reasonable estimation for the bond-slip model, as a function of the corrosion level.

- The dilatation component $\mathcal{D}$, utilized in the mesoscopic plane strain model, is computed from equation (20). Following [29] and [19] we adopt the relation: $R_f = R_i + X$, which is based on the incompressibility assumption of the corrosion products. For each solved case, the X value is adopted from Table 5, columns 2-4.

- Finally, the steel yield stress (σ_Y) is reported in Table 4, column 7. The reinforcement cross section reduction, due to corrosion, is computed assuming an effective bar radius $R_{eff} = R_i - X$. Note that both characterizations apply only to the structural member analysis.

5.2 Numerical results: the mesoscopic cross section model

In this Section, we describe the obtained numerical results related to the expansion mechanism of steel bars for a predefined corrosion attack depth, and the degradation induced in concrete at the cross section level.

The sequence of Figures 9-11 shows, for the beam type 11 at the final stage of analysis, the iso-displacement contour lines, the FE mesh in the (scaled) deformed configuration and the damage distribution in the cross section. A complete degradation of the surrounding concrete is observed for the applied expansion levels. It can be noted that the main local failure mechanism is an inclined crack pattern.

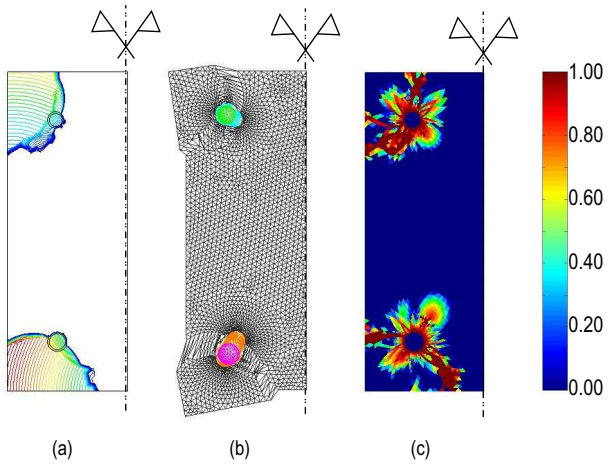

Figure 9: Plane strain expansion analysis. Beam type 11-4: (a) Iso-displacement contour lines (pattern of cracks). (b) Scaled deformed configuration. (c) Damage contour fill.

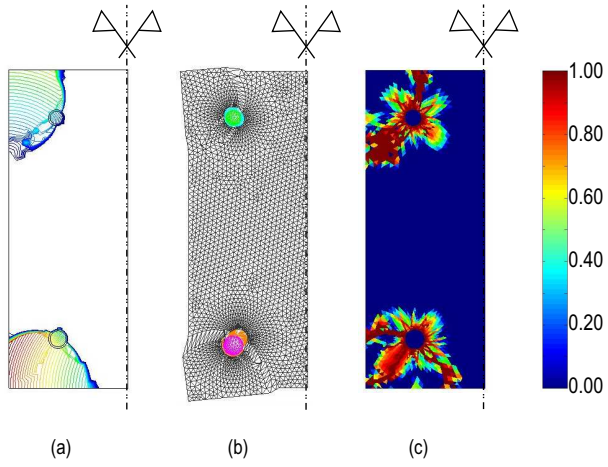

Figure 10: Plane strain expansion analysis. Beam type 11-5: (a) Iso-displacement contour lines (pattern of cracks). (b) Scaled deformed configuration. (c) Damage contour fill.

Figures 12-13 show, for the beam type 31 and at the final stage of analysis, the iso-displacement contour lines, the deformed (scaled) configuration and the damage map. A complete concrete degradation around the bars is observed. In this case, the local failure mechanism consists of delamination, between adjacent bars, and inclined cracking for the extreme steel fibers.

In general, at the cross section level and from a qualitative point of view, it can be observed that the proposed mesoscopic plane strain numerical model captures physically admissible failure mechanisms. The introduction of friction-contact (interface) finite elements in the simulations has been a key point in order to obtain consistent patterns of cracks.

Also, it can be mentioned that the obtained pattern of fractures matches very well with the semi-analytical predictions taken from Capozucca [21] (which were deduced from the physical mathematical model developed by Bazant [13, 14]):

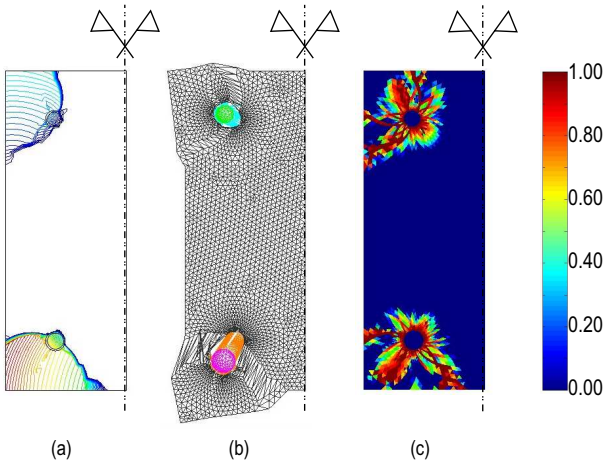

Figure 11: Plane strain expansion analysis. Beam type 11-6: (a) Iso-displacement contour lines (pattern of cracks). (b) Scaled deformed configuration. (c) Damage contour fill.

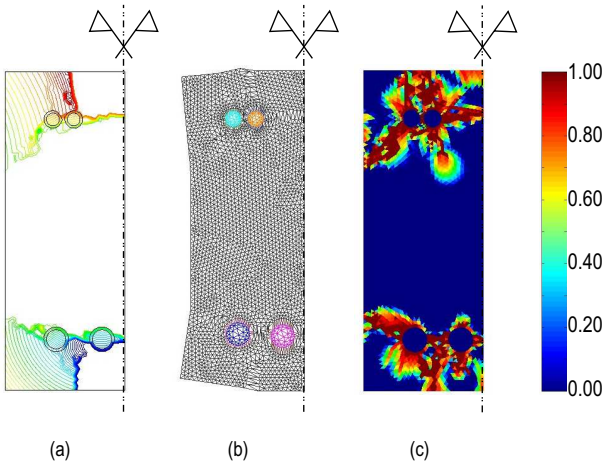

Figure 12: Plane strain expansion analysis. Beam type 31-3: (a) Iso-displacement contour lines (pattern of cracks). (b) Scaled deformed configuration. (c) Damage contour fill.

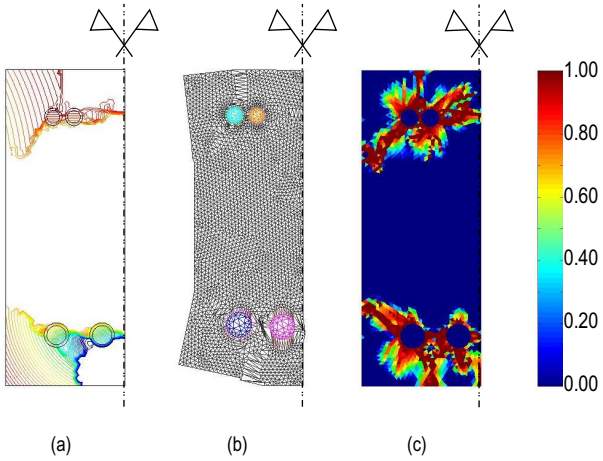

Figure 13: Plane strain expansion analysis. Beam type 31-4: (a) Iso-displacement contour lines (pattern of cracks). (b) Scaled deformed configuration. (c) Damage contour fill.

$$\text{if } S > (6D) \quad \rightarrow \text{inclined cracking prevails}$$
$$\text{if } L > \frac{(S-D)}{2} \quad \rightarrow \text{delamination mechanism prevails}$$

where S is the horizontal spacing of bars, D the diameter of the reinforcement bars and L the cover depth.

5.3 Numerical results: the mesoscopic bending model

The main quantitative result of the previous analysis is the value of the damage variable at the whole cross section. Taking into account the coupling philosophy described in Section 4, this information is post-processed in order to impose an initial degradation condition for the RC members and a subsequent structural analysis is performed using the model discussed in Section 3. Here, we show the main results of this approach.

Figures 14-15 depict the obtained damage distribution, the trajectory of active macro cracks at the end of the simulation as iso-displacement contour lines (in the z-direction) and the contour fill of the axial σ_{zz} stress, for two of the beams type 11 (the not corroded case 11-1 and the corroded one 11-4, from Table 5).

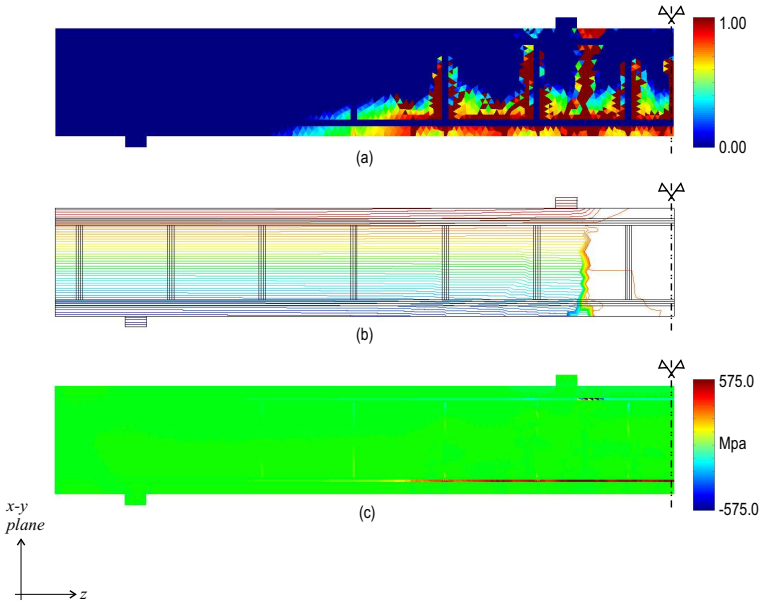

Figure 14: Qualitative results for the plane stress mesoscopic model. Beam type 11-1 (not corroded case): (a) Final contour fill of damage. (b) Iso-displacement contour lines in z-direction. (c) Contour fill of σ_{zz}.

The same analysis, of the obtained numerical results, can be applied to beam type 31, see Figures 16-17.

In all the studied cases a vertical macro crack, located at the center of the beam, has been identified as the fundamental macroscopic ultimate mechanism determining the limit load. It is characterized by a mode I of fracture, which is the typical ones for those cases of slightly RC beams. No macroscopic bond-slip failure mechanism has been detected in any of the analyzed tests. These facts suggest that, for this particular beams, a simpler concept could be applied in order to estimate the ultimate resistance, as for example any of the classical methodologies adopted in the concrete design codes for RC cross sections. In this context of analysis, whenever a standard code procedure is utilized, the problem consists of taking into account (correctly) the influence of the degradation process induced by the corrosion rebar. In Appendix A, we propose a simple strategy to reach this objective, using the information derived from the plane strain cross section mesoscopic model and the guidelines of a particular RC design code (DIN-1045 [30, 31]).

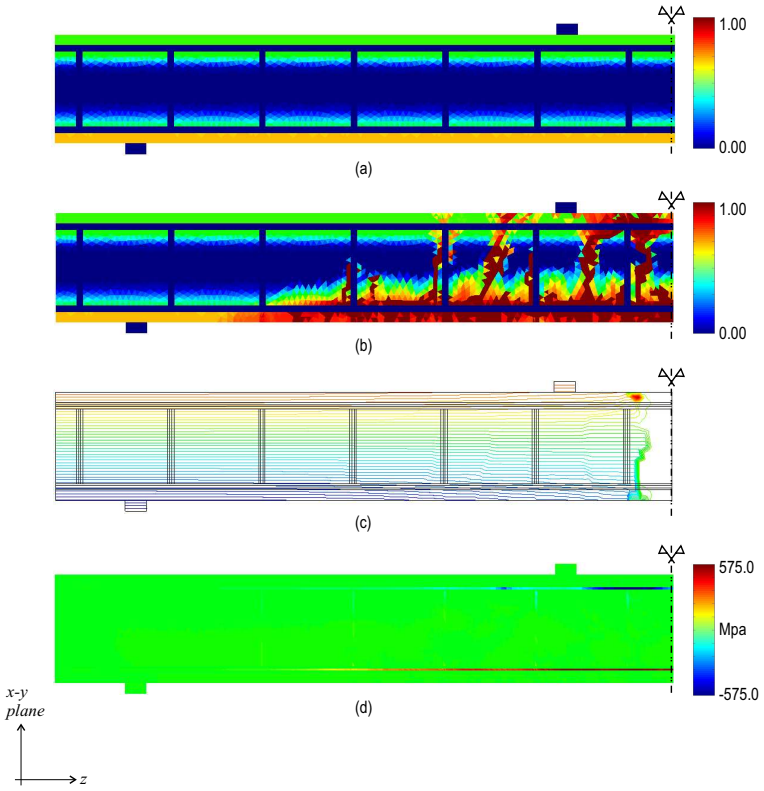

Figure 15: Qualitative results for the plane stress mesoscopic model. Beam type 11-4: (a) Initial damage condition. (b) Final contour fill of damage. (c) Iso-displacement contour lines in z-direction. (d) Contour fill of σ_{zz}.

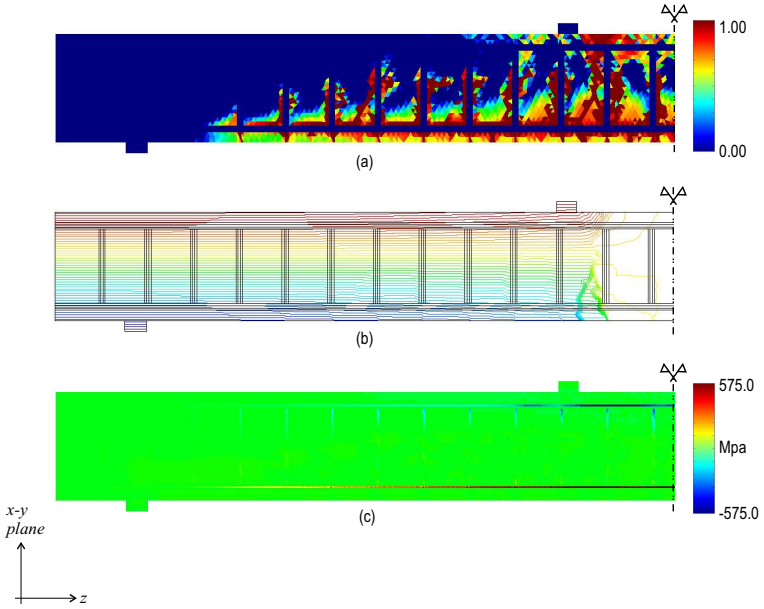

Figure 16: Qualitative results for the plane stress mesoscopic model. Beam type 31-1 (not corroded case): (a) Final contour fill of damage. (b) Iso-displacement contour lines in z-direction. (c) Contour fill of σ_{zz}.

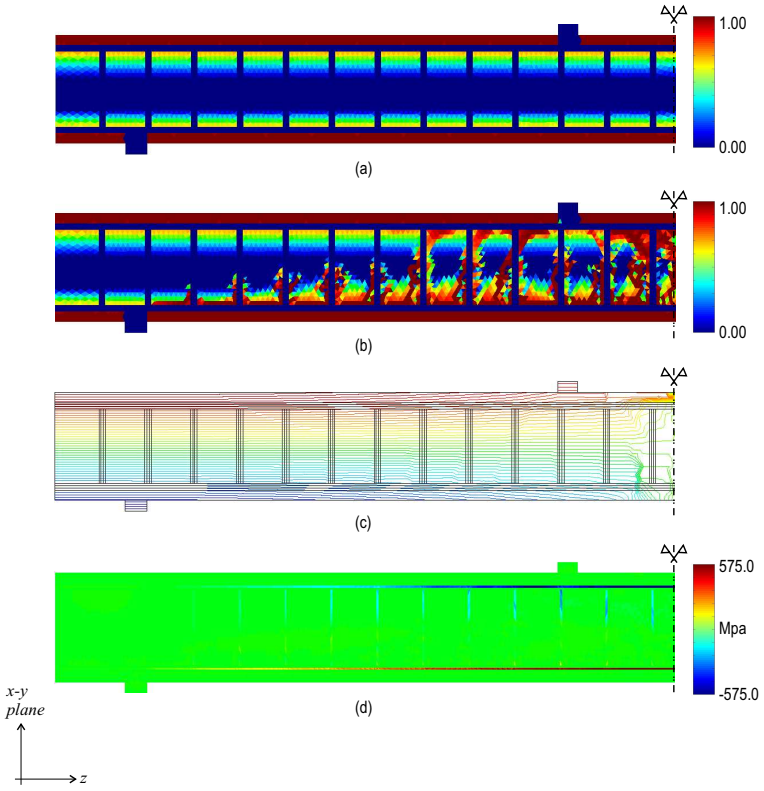

Figure 17: Qualitative results for the plane stress mesoscopic model. Beam type 31-3: (a) Initial damage condition. (a) Final contour fill of damage. (b) Iso-displacement contour lines in z-direction. (c) Contour fill of σ_{zz}.

In the Figures 18-24 we show the evolution of the total vertical load vs. the mid span vertical displacement curves, obtained using the proposed mesoscopic model, for the beam type 11 and 31. Those curves are contrasted with experimental (Rodriguez et al. [4]) and numerical results (Coronelli et al. [19]). A good agreement with them has been obtained. In general, we note a better adjustment of our numerical results, if compared with the experimental ones, than that presented by Coronelli et al. [19].

It can be seen that the typical behavior of the RC beams is appropriately captured, i.e. the the existence of three well defined slopes in the mechanical responses (see Figures 18-24): an initial stiffness associated with the undamage state (without cracks) in the concrete, an intermediate stiffness characterizing the evolution and propagation of multiple tensile macro-fractures in the concrete and a (horizontal) final slope which defines the limit mechanism of failure due to reaching either the ultimate compressive strength of concrete or yielding in the steel reinforcements.

These figures also depict the limit loads computed following the DIN-1045 code hypothesis (see appendix A), for two situations: *(i)* considering an initial damage distribution in the concrete matrix due to corrosion and *(ii)* vanishing completely the concrete contribution in the limit equilibrium.

As we expected, the proposed mesoscopic numerical strategy matches very well the obtained limit load predictions using the DIN code solution. Similar conclusions should be obtained if a different design code would have been used. This concordance can be justified as follows: *(i)* in all the tests, the obtained failure mechanism using the mesoscopic model corresponds to an identical failure mode assumed in the code at equilibrium limit state (mode I of fracture), *(ii)* the main hypothesis introduced by the RC design codes is the Bernoulli-Navier's kinematic restriction (plane cross section remains as plane cross sections) which, for these particular beams, seems to be valid because no macroscopic bond-slip failure has been detected in the numerical model, and finally *(iii)* similar constitutive laws (in both approaches) are used, indeed equal ultimate strengths have been adopted for the concrete and steel reinforcements.

It must be noted that this comparison in terms of limit loads, between the mesoscopic strategy and the code procedure guidelines, has been included in order to show the mathematical consistency of the present FE approach. In general cases, more complex (or even coupled) mechanisms of failure could be

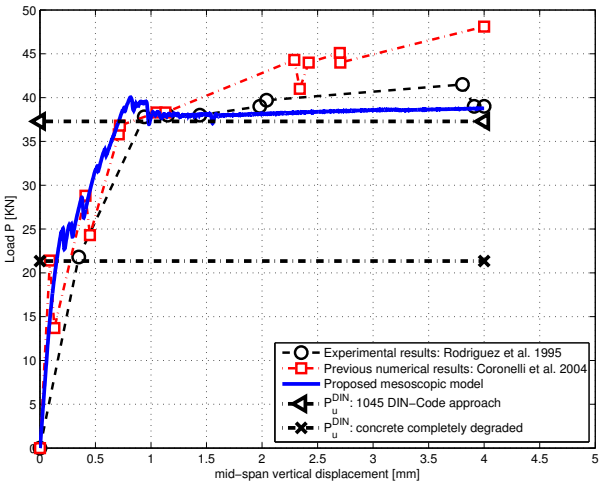

Figure 18: Load vs. displacement structural response. Beam type 11-1.

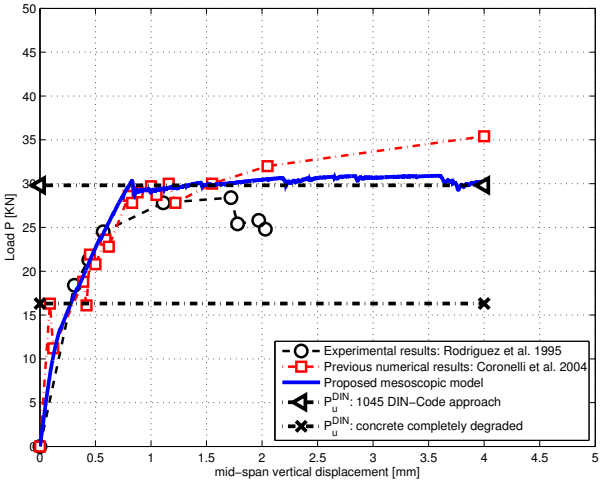

Figure 19: Load vs. displacement structural response. Beam type 11-4.

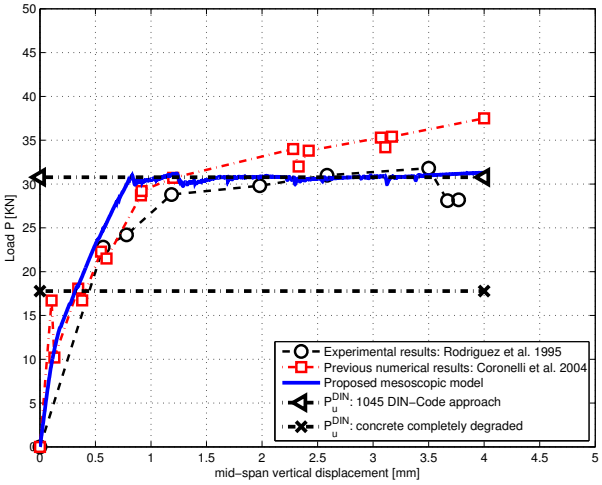

Figure 20: Load vs. displacement structural response. Beam type 11-5.

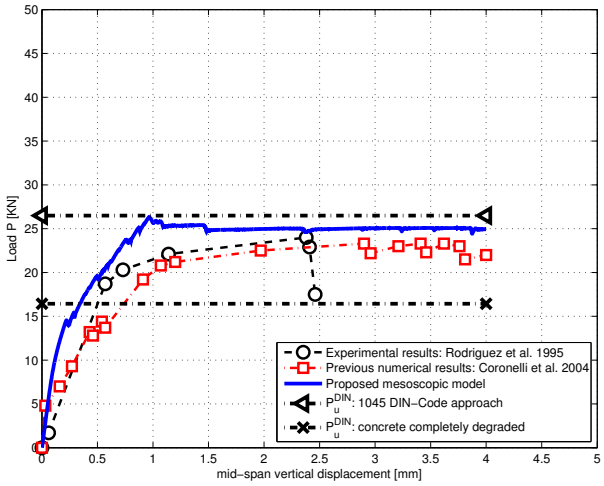

Figure 21: Load vs. displacement structural response. Beam type 11-6.

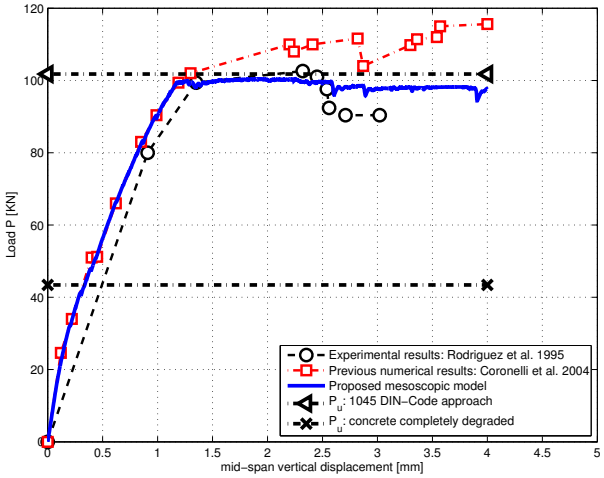

Figure 22: Load vs. displacement structural response. Beam type 31-1.

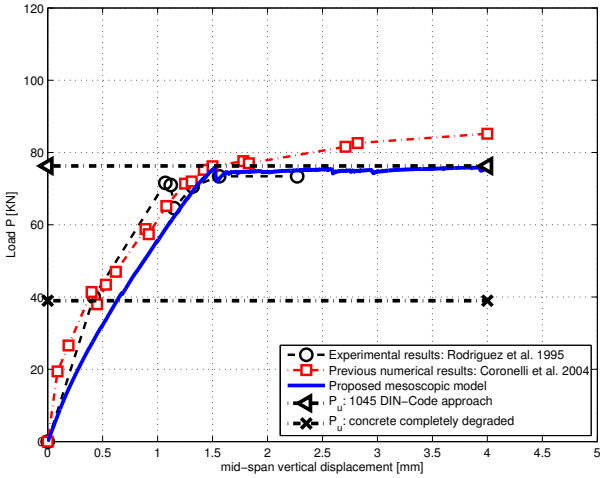

Figure 23: Load vs. displacement structural response. Beam type 31-3.

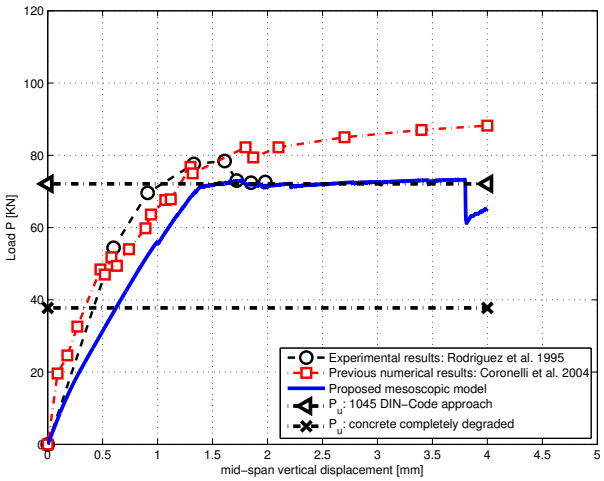

Figure 24: Load vs. displacement structural response. Beam type 31-4.

developed in the RC structure where only numerical predictions can be obtained.

In Figures 25-26, we superpose the sequence of responses for each beam type (11 and 31) when the proposed mesoscopic model is used. The loss of carrying load capacity and structural stiffness degradation, in terms of the degree of corrosion attack, can be clearly observed.

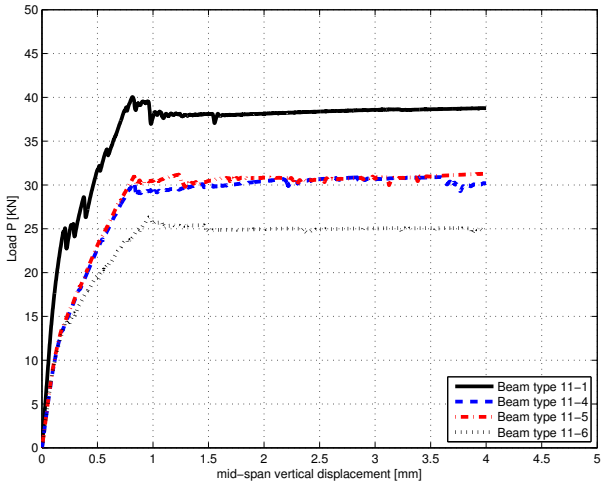

Figure 25: Load vs. displacement structural response. Beams type 11.

6 Conclusions

Throughout the paper, we have presented an application of the *CSDA* to solve RC structural problems undergoing a rebar corrosion phenomenon. As a novel contribution, two different mesoscopic size-scale model have been developed: at cross section level and at global or structural level. A coupling strategy between them has also been proposed.

Contact finite elements were introduced in these formulations in order to improve the simulation of the steel-concrete interface effects. Following the proposed methodology, the most relevant corrosion mechanisms can be simulated, as for example: expansion of steel bars, damage/cracking in the concrete, yielding in the reinforcements, bond stress degradation at the interface and steel cross section reduction.

Because the model offers information in all the stages of the degradation process (continuous evaluation of the structural strength deterioration) it could be used not only to compute limit states, but also to predict possible mechanisms that affect the structural *serviceability* for a hypothetical level of corrosion. In summary, it represents a viable technique to analyze deteriorated RC members.

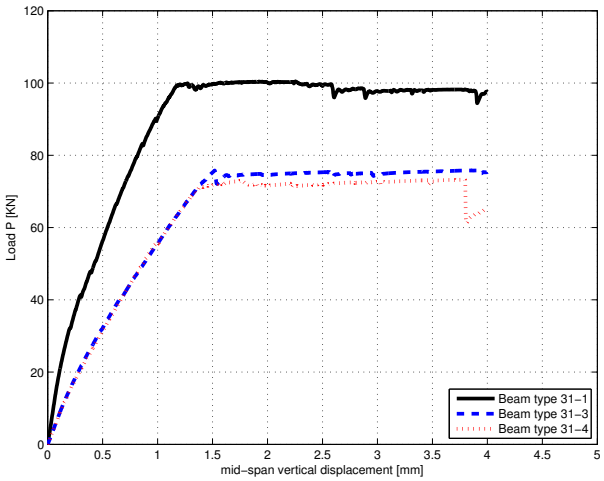

Figure 26: Load vs. displacement structural response. Beams type 31.

Additional conclusion that can be obtained from the numerical simulations are:

- The mesoscopic plane strain model of the cross section captures adequately the experimental crack patterns. Inclined cracking or delamination modes have been obtained, depending on the location and separation of reinforcement bars. The proposed model can be applied to more sophisticated RC cross section geometrical designs to obtain a qualitative idea of the deterioration mechanisms induced by the expansion-corrosion process.
- At the structural level, the mesoscopic plane stress model captures physically admissible concrete degradation patterns. In all the analyzed cases, a typical mode I of fracture, characterizing the final macroscopic failure mechanism, has been observed. The sensitivity of the limit load evaluations with the reinforcement corrosion level has been acceptably computed.

Acknowledgements

Financial support from the Spanish Ministry of Science and Technology trough grant BIA2005-09250-C03-03 and from ANPCyT of Argentina through grant PICT-2005- 34273, are gratefully acknowledged.

A Appendix: Ultimate load estimation for corroded RC members using design code guidelines and a pre-defined level of damage at the cross section

To determine the limit relation between the ultimate internal bending moment ($\boldsymbol{M}_u^{int}$) and the ultimate internal axial strength ($\boldsymbol{N}_u^{int}$), for a given RC cross section, the modern codes of design are based in the following four key assumptions:

- The applicability of Navier-Bernoulli's hypothesis until reaching the failure.
- A set of pre-defined limit deformation kinematics states (planes in this case).
- The adoption of adequate non-linear inelastic constitutive models for the concrete and steel.
- Limit equilibrium conditions between the resultant external loads $\boldsymbol{M}_u^{ext}$-$\boldsymbol{N}_u^{ext}$ (see Figure 27-(b)) and the internal generalized forces $\boldsymbol{M}_u^{int}$-$\boldsymbol{N}_u^{int}$ induced in the composite material.

Depending on the particular definition adopted for every one of this items, different code procedures can be recovered. For the purposes of the present work, the DIN-1045 code guidelines are adopted [30, 31]. The main considerations introduced by this particular approach, in terms of the pre-defined limit kinematics states and material constitutive behavior, can be seen in Figures 27-(c), 28-(a) and 28-(c). We also propose a generalization of such normalized procedure in order to take into account the degradation induced by the rebar corrosion. It is assumed that the corrosion attack depth "X" is a know input data parameter. The proposed methodology is based on the following aspects: *(a)* the contribution of each steel bar reinforcement B^i is modelled by means of its net cross section $\Omega^i = \pi R^2_{eff}$, i.e. the effective bar radius is used (see sub-Section 5.1); *(b)* the cross section of the concrete domain is considered as the sum of several disjunct rectangular layers C^j ($\Omega^j = b^j\, h^j$ being its area contribution) as Figure 28-(b) shows; *(c)* each one of that concrete layers (C^j) is characterized by a *degraded constitutive response* (see Figure 28-(a)) which depends on the average damage distribution obtained using the mesoscopic plane strain model of Section 2; *(d)* loss of adherence cannot be introduced in this approach, this fact reveals a limitation of this methodology for more general situations. Note that the supra-indices i and j have been used in order to denote each steel fiber and concrete layer, respectively.

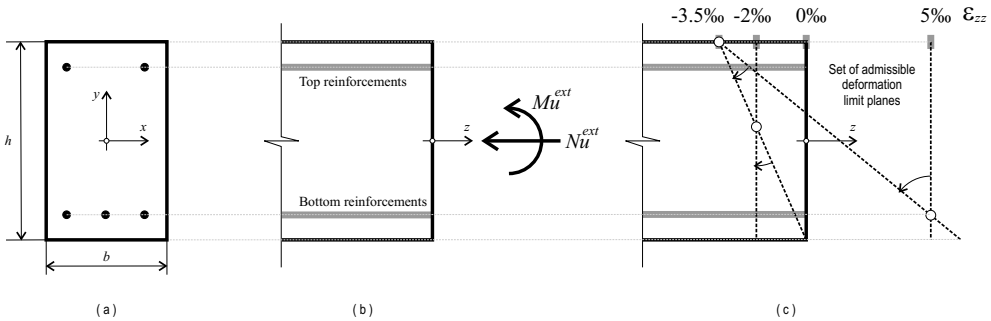

Figure 27: DIN-1045 code guidelines: (a) Cross section of a typical RC member. (b) Scheme of the ultimate axial-bending external loads. (c) Pre-defined set of kinematics limit states.

In view of the above mentioned ingredients, a simple iterative procedure (in terms of the admissible limit kinematics of Figure 27-(c)) can be formulated to solve the following ultimate equilibrium conditions:

$$\begin{aligned} \boldsymbol{M}_u^{int} + \boldsymbol{M}_u^{ext} = 0 \quad \rightarrow \quad & \overbrace{\sum_{i=1}^{n_B} \left[\Omega^i\, \sigma^i_{zz}\, y^i\right]}^{\textit{T1}\text{: steel contribution}} + \overbrace{\sum_{j=1}^{n_C} \left[\Omega^j\, \sigma^j_{zz}\, y^j\right]}^{\textit{T2}\text{: concrete contribution}} + \boldsymbol{M}_u^{ext} = 0 \\ \boldsymbol{N}_u^{int} + \boldsymbol{N}_u^{ext} = 0 \quad \rightarrow \quad & \underbrace{\sum_{i=1}^{n_B} \left[\Omega^i\, \sigma^i_{zz}\right]}_{\textit{T1}\text{: steel contribution}} + \underbrace{\sum_{j=1}^{n_C} \left[\Omega^j\, \sigma^j_{zz}\right]}_{\textit{T2}\text{: concrete contribution}} + \boldsymbol{N}_u^{ext} = 0 \end{aligned} \tag{35}$$

where σ_{zz} denotes the stress component normal to the cross section of the RC member, n_B and n_C are the number of total steel bars and concrete layers, respectively. Also we have defined y^i and y^j as the adequate distances (for each bar and concrete layer) to compute the internal bending moments. In this particular case, the ultimate internal bending moment ($\boldsymbol{M}_u^{int}$) is computed with respect to the gravity center of the cross section (G), see Figure 28-(b).

It should be noted that, in the studied tests and from the external load state showed in Figure 8-(a), the uniqueness of solution for the system (35) is recovered by imposing the following additional restriction: $\boldsymbol{N}_u^{ext} = 0$. Finally, an estimation for the ultimate limit load can be easily computed as:

$$P_u^{DIN} = \frac{2\boldsymbol{M}_u^{int}}{a} \tag{36}$$

where a is the distance showed in Figure 8-(a).

Figures 18-24, in Section 5.3, depict the values obtained when equation (36) is applied, for each beam case. The lower values, also displayed in those Figures, correspond to the (hypothetical) solution without the concrete contribution, i.e. $T2 \equiv 0$ in equations (35).

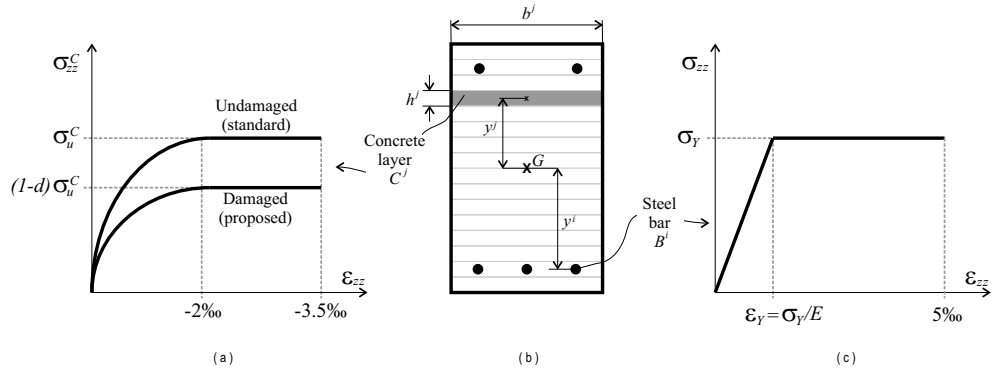

Figure 28: DIN-1045 code guidelines: (a) Modified (proposed) constitutive model for each layer of concrete C^j as a function of the damage value "d". (b) Idealized layer discretization of the cross section. (c) Constitutive model (isotropic) for each fiber of reinforcement B^i.

References

[1] J. Cairns and S. Millard. Section 13.2: Reinforcement corrosion and its effects on residual strength of concrete structures. In M. Forde, editor, *Proc. 8^{th} Int. Conf. on Structure Faults and Repair 99*, pages (CD–ROM), Edinburgh, U.K., 1999. Engineering Tech. Press.

[2] D. Chen and S. Mahadevan. Chloride-induced reinforcement corrosion and concrete cracking simulation. *Cement & Concrete Composites*, in press, 2007.

[3] J. Rodriguez, L. Ortega, and A. Garcia. Corrosion of reinforcing bars and service life of r/c structures: Corrosion and bond deterioration. In *Proc. Int. Conf. on concrete across Borders*, volume 2, Odense, Denmark, 1994.

[4] J. Rodriguez, L. Ortega, and J. Casal. Load carrying capacity of concrete structures with corroded reinforcement. In M. Forde, editor, *4^{th} Int. Conf. on Structure Faults and Repair*, pages 189–199, Edinburgh, U.K., 1995. Engineering Tech. Press.

[5] J. Rodriguez, M. Ortega, J. Casal, and M.D. Diez. Assesing structural conditions of concrete structures with corroded reinforcement. In R.K. Dhir Dundee, Scotland and N.A. Henderson, editors, *Proc. Int. Conf. on Concrete in the Service of Mankind*, pages 141–150, London, 1996. E&FN Spon.

[6] K. Okada, K. Kobayashi, and T. Miyagawa. Influence of longitudinal cracking due to reinforcement corrosion on characteristics of reinforced concrete members. *ACI Struct. J.*, 85(2):134–140, 1988.

[7] T. Uomoto and S. Misra. Behaviour of concrete beams and columns in marine environments when corrosion of reinforcing bars takes place. *ACI Special Publication*, SP-109:127–145, 1988.

[8] Y. Tachibana, K.I. Maeda Y. Kajakawa, and M. Kawamura. Mechanical behaviour of rc beams damage by corrosion of reinforcement. In *Proc. 3^{dr} International Symposium on Conrrosion of Reinforcement in Concrete Construction*, pages 178–187, Wishaw, UK, 1990.

[9] J.G. Cabrera and P. Ghoddoussi. The effect of reinforcement corrosion on the strength of the steel/concrete bond. In *Proc. Int. Conf. on Bond in Concrete*, pages 10/11–10/24, Riga, Latvia, 1992. CEB.

[10] A.A. Almusallam, A.S. Al-Gahtani, A.R. Aziz, and Rasheeduzzafar. Effect of reinforcement corrosion on bond strength. *Constr. Build. Mater.*, 10(2):123–129, 1996.

[11] G.J. Al-Sulaimani, M. Kaleemullah, I.A. Basumbul, and Rasheeduzzafar. Influence of corrosion and cracking on bond behavior and strength of reinforced concrete members. *ACI Struct. J.*, 87(2):220–231, 1990.

[12] R. Huang and C.C. Yang. Condition assessment of reinforced concrete beams relative to reinforcement corrosion. *Cement & Concrete Composite*, 19:131–137, 1997.

[13] Z.P. Bazant. Physical model for steel corrosion in concrete sea structures - theory. *J. Struct. Div.*, pages 1137–1153, 1979.

[14] Z.P. Bazant. Physical model for steel corrosion in concrete sea structures - applications. *J. Struct. Div.*, pages 1155–1165, 1979.

[15] K. Bhargava, A.K. Ghosh, Y. Mori, and S. Ramanujam. Model for cover cracking due to rebar corrosoin in rc structures. *Engineering Structures*, 28:1093–1109, 2006.

[16] K. Bhargava, A.K. Ghosh, Y. Mori, and S. Ramanujam. Corrosion-induced bond strength degradation in reinforced concrete- analitical and empical models. *Nuclear Engineering and Design*, 237:1140–1157, 2007.

[17] F.J. Vecchio. Nonlinear finite element analysis of reinforced concrete: At the crossroads? *Struct. Concr.*, 2(4):201–212, 2001.

[18] A. Castellani and D. Coronelli. Section 13.7: Beams with corroded reinforcement: Evaluation of effects of cross section losses and bond deterioration by finite element analysis. In M. Forde, editor, *Proc. 8^{th} Int. Conf. on Structure Faults and Repair 99*, pages (CD–ROM), Edinburgh, U.K., 1999. Engineering Tech. Press.

[19] D. Coronelli and P. Gambarova. Structural assessment of corroed reinforced concrete beams: modeling guidelines. *J. Struct. Eng. ASCE*, 130(8):1214–1224, 2004.

[20] C. Fang, K. Lundgren, M. Plos, and K. Gylltoft. Bond behaviour of corroded reinforcing steel bars in concrete. *Cement and Concrete Research*, 36:1931–1938, 2006.

[21] R. Capozucca. Damage to reinforced concrete due to reinforcement corrosion. *Construction and Building Materials*, 9(5):295–303, 1995.

[22] J. Oliver, A. E. Huespe, M. D. G. Pulido, and E. Chaves. From continuum mechanics to fracture mechanics: the strong discontinuity approach. *Engineering Fracture Mechanics*, 69:113–136, 2002.

[23] J. Oliver and A.E. Huespe. Theoretical and computational issues in modelling material failure in strong discontinuity scenarios. *Comput. Meth. App. Mech. Eng.*, 193:2987–3014, 2004.

[24] J. Oliver and A. E. Huespe. Continuum approach to material failure in strong discontinuity settings. *Comp. Meth. Appl. Mech. in Engrg.*, 193:3195–3220, 2004.

[25] J. Oliver, M. Cervera, S. Oller, and J. Lubliner. Isotropic damage models and smeared crack analysis of concrete. In *N.B. et al. editor, SCI-C Computer Aided Analysis and design of concrete Structures*, pages 945–957, Swansea, 1990. Pineridge Press.

[26] J. Oliver. On the discrete constitutive models induced by strong discontinuity kinematics and continuum constitutive equations. *Int. J. Solids Struct.*, 37:7207–7229, 2000.

[27] J. Oliver, A.E. Huespe, and P.J. Sánchez. A comparative study on finite elements for capturing strong discontinuities: e-fem vs x-fem. *Comput. Methods Appl. Mech. Engrg.*, 195(37-40):4732–4752, 2006.

[28] J. Oliver, A. E. Huespe, and J. Cante. An implicit/explicit integration scheme to increase computability of non-linear material and contact/friction problems. *Comp. Meth. Appl. Mech. in Engrg.*, In press, Corrected proof. Available on line 8 December, 2007.

[29] F.J. Molina, C. Alonso, and C. Andrade. Cover cracking as a function of rebar corrosion. II: Numerical model. *Mater. Struct.*, 26:532–548, 1993.

[30] *DIN 1045*. Beton und Stahlbeton, 1988.

[31] V. F. Leonhardt and E. Möning. *Vorlesungen über Massivbau. Teil 1. Grundlagen zur Bemessung im Stahlbetonbau*. Springer-Verlag Berlín, Heidelberg, 1984.